

# Additively Manufactured and Self Activating Hybrid Demisable Joint Design for Large Satellite Platforms

Alexander Ring<sup>(1)</sup>, Isil Sakraker-Özmen<sup>(1)</sup>, Simon Hümbert<sup>(1)</sup>, Tobias Lips<sup>(2)</sup>, Frank Blender<sup>(3)</sup>

(1) Deutsches Zentrum für Luft- und Raumfahrt e.V. (DLR), Pfaffenwaldring 38-40, 70569 Stuttgart, Germany, [alexander.ring@dlr.de](mailto:alexander.ring@dlr.de); [isil.sakraker@dlr.de](mailto:isil.sakraker@dlr.de); [simon.huembert@dlr.de](mailto:simon.huembert@dlr.de)

(2) HTG – Hyperschall Technologie Göttingen GmbH, Am Handweisergraben 13, 37120 Bovenden, Germany [t.lips@htg-gmbh.com](mailto:t.lips@htg-gmbh.com)

(3) Airbus Defence and Space GmbH, Claude-Dornier-Strasse, 88090 Immenstaad a.B., Germany [frank.blender@airbus.com](mailto:frank.blender@airbus.com)

## ABSTRACT

The increasing number of rocket-launches and satellite constellations has heightened concerns over space debris and the risks associated with uncontrolled atmospheric re-entry. Design for Demise (D4D) aims to mitigate these risks by ensuring satellite structures disintegrate at high altitudes, reducing debris casualty area (DCA). This study investigates novel demisable joint concepts for primary satellite structures, utilizing additively manufactured inserts complemented by passive ejection mechanisms such as Shape Memory Alloy (SMA) actuators and compression springs. Using ESA's Sentinel-6 (S6) mission as a reference, hybrid-material joints were designed, analyzed, and tested. Simulations demonstrated their ability to withstand launch loads. Re-entry analysis and thermal simulations indicated structural breakup at altitudes up to 115 km, achieving a 60% reduction in DCA area compared to the reference configuration without demisable joints. Physical prototypes tested at DLR facilities validated these findings. The results demonstrate the effectiveness of demisable joints in enhancing satellite structural breakup during re-entry, contributing to improved space debris mitigation.

## 1 INTRODUCTION

Since the launch of Sputnik 1 in 1957, the number of objects in space has grown significantly. Advances in technology and reduced launch costs, driven by innovations like reusable rockets, have led to a surge in satellite deployments, especially for communication and Earth observation [1].

The growing number of space objects is driven not only by new launches but also by collisions, anti-satellite tests, and mission-related debris. Many of these objects remain untracked, but statistical models estimate around 40,500 debris pieces larger than 10 cm [2]. Efforts to address space debris include short-term measures, such as reducing mission-related debris, and long-term solutions like active debris removal and satellite deorbiting. NASA

first identified the space debris threat in the 1990s and developed mitigation guidelines that have since evolved. At the end of their mission, satellites are either deorbited or relocated to graveyard orbits to prevent cascading collisions in congested orbital regions, a phenomenon first described by Kessler in 1978 [3]. Re-entering space debris poses safety risks, requiring adherence to established thresholds. NASA set a human casualty risk limit of 1:10,000 for re-entry events, a standard adopted by other agencies, including ESA. D4D improves spacecraft demisability, reducing the amount of surviving debris. ESA has promoted D4D through its Clean Space initiative since 2012. Studies show that controlled dismantling significantly reduces DCA, emphasizing D4D's role in ensuring the long-term sustainability of space operations [4].

The aim of this work is to build upon previous research at DLR-BT and develop a new hybrid and 3D-printed metal-thermoplastic demisable joint concept, using programmable materials, that is passively triggered at a higher altitude than it would naturally disintegrate, to ensure an early break-up of the primary structure.

## 2 REFERENCE MISSION

The selection of a reference mission for this study is based on key factors influencing spacecraft demise, including geometry, mass, material properties, and orbit characteristics. Hard-to-demise components are typically large, heavy, and made of high-melting-point materials. Generally, satellites exceeding 500 kg pose a human casualty risk above  $10^{-4}$  [5].

Access to detailed satellite data is crucial for designing and evaluating novel demisable structural joints. However, such data is often confidential, requiring collaboration with a satellite manufacturer. After assessing multiple candidates based on availability and feasibility, the S6 mission was selected. The S6 satellite, developed by NASA, ESA, EUMETSAT, and NOAA, is manufactured by Airbus Defense and Space in Friedrichshafen, Germany, which agreed to provide model data under a non-disclosure agreement. While this

study utilizes S6 as a baseline, the analysed reference model remains independent of the actual mission, yet sufficiently similar. The reference satellite is employed in re-entry simulations to assess the impact of demisable structural joints on overall spacecraft demise. It provides critical structural and load data derived from its detailed model and launch specifications. Due to the structural similarities among large satellites, the proposed concepts can be adapted for various mission profiles.

S6, part of ESA's Copernicus Earth observation program, consists of two identical satellites launched in 2020 and 2025 [6]. Figure 1 shows an artist impression of the S6 satellite in orbit. The 1362 kg heavy satellite operates in a 1336 km prograde orbit with a 66° inclination. Its primary structure comprises aluminium honeycomb sandwich panels made with the following specifications: 0.5 mm thick aluminium face sheets combined with a Hexcel™ 5056 aluminium honeycomb core with 3/16-inch cell size and 0.001 inches foil thickness. The panels feature core heights of 19, 24 and 29 mm. These characteristics make it a suitable candidate for evaluating advanced demisability techniques.



Figure 1. Artist Impression of the S6 Satellite in Orbit [ESA].

### 3 DEMISABLE JOINT DESIGN

#### 3.1 Previous Work

Since 2020, several studies at DLR-BT have explored demisable structural joints for primary satellite structures. Prior concepts include additively manufactured (AM) thermoplastic patches, spring-loaded mechanisms, and programmable materials. Patzwald's AM thermoplastic patch design improved break-up altitude, demonstrating the benefits of AM materials for post-mission disposal [7]. Brodbeck's multi-material insert, combining PEEK and PEI with a helical spring, aimed to mitigate non-separation risks [8]. However, it exhibited structural weaknesses and overlooked system-level dynamics.

Other studies investigated easy-to-demise materials. Grassi et al. introduced washers made of zinc- and tin-based alloys. Plasma wind tunnel tests showed partial success, but separation issues arose due to molten material viscosity and aerodynamic forces [9]. Similarly,

Sauerbrey et al. conducted 38 tests on various D4D techniques, evaluating demisability, spacecraft impact, and safety [10]. Among tested concepts, a redesigned insert showed controlled breakage at a specific temperature, ensuring joint release. A CFRP PEEK composite insert aimed to lower melting temperature but failed to enhance demise behaviour. The SMA-based concept, using shape-memory alloys to fracture bolts, enabled the fastest panel release but resulted in significant mass increase. These findings informed the development of the novel concept of Ring, presented in this paper [11].

#### 3.2 Hybrid Demisable Joint (HDJ) Concept

The HDJ design prioritizes compatibility with existing satellite assembly, integration, and testing (AIT) processes. As sandwich panels form the primary satellite structure, the focus is on bolted and bonded joining methods. Common configurations include L-joints, where brackets secure outer panels, and T-joints, where inner panels connect via brackets or threaded inserts. Figure 2 illustrates these methods. Drawing from satellite fastening solutions and expert consultations, the HDJ aims to provide a universally applicable approach for structural sandwich panel connections, specifically addressing the primary L- and T-joint structures found in the S6 satellite. Therefore, two distinct joint design will be derived from the specifications.

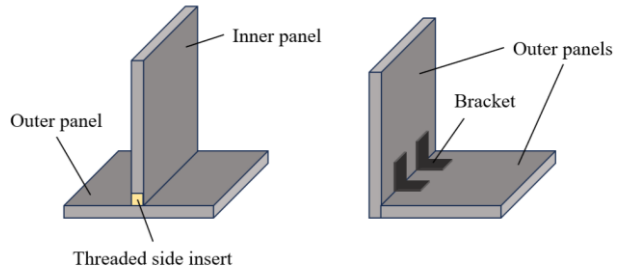


Figure 2. T-joint panel connection (left), L-joint panel connection with brackets (right).

##### 3.2.1 Material Selection

The material selection for the HDJ is based on the employed D4D technology and demisability concept. Building on previous research, the most promising approaches include demisable inserts, SMA actuators, and composite materials. The total heat load per unit area required for demise follows Eq. 1, dependent on mass, surface area, and specific enthalpy of ablation. This enthalpy is derived from material properties such as specific heat capacity, melting temperature, and enthalpy of fusion, see Eq. 2.

$$Q = \frac{m \cdot h_a}{A_s} \quad (1)$$

$$h_a = c_p(T_m - T_i) + h_f \quad (2)$$

A sensitivity analysis by Patzwald examined the influence of design parameters on convective heat per unit area. By splitting total heat into convective and reradiated components, Eq. 3 was formulated. The analysis, shown in Table 1, ranks parameter influence, normalized to mass. Melting temperature and specific heat capacity significantly impact demise behaviour, followed by surface area. Emissivity has a contributing effect of only 8% of mass influence.

$$Q_{cw} > \frac{m[c_p(T_m - T_i) + h_f]}{A_s} + \frac{\varepsilon Q_{rr}}{A_s} \quad (3)$$

Since satellite components are designed for extreme lightweight construction, reducing mass via geometry changes is impractical. Instead, optimizing material properties—especially thermal characteristics and density—offers the highest potential for increasing break-up altitude, making it a key factor in HDJ design.

Table 1. Magnitude of influence of different design parameters on the convective heat.

Parameter	Influence $i_m$
$m$	1
$T_m$	0.89
$c_p$	0.56
$A_s$	0.50
$h_f$	0.44
$T_i$	0.31
$\varepsilon$	0.08

The high-performance thermoplastics PEEK and PEI feature the most promising properties for structural aerospace applications. Both the density and thermal properties show significant benefits compared to conventional metals like aluminium alloys, stainless steel, and titanium in terms of demisability. The expertise and easy availability make them excellent choices for this work. The filaments are available both as pure thermoplastic material as well as reinforced with chopped carbon fibres to improve mechanical properties.

### 3.2.2 Mechanism

The HDJ design features a two-stage passive temperature-triggered screw ejection mechanism. Initially, the force-fit connection between the connected panels is loosened as the thermoplastic material reaches its heat deflection temperature (HDT). PEI without carbon fibre reinforcement features the lowest HDT out of the available materials at 158 °C, thus representing the best candidate for this purpose.

In a second stage, the screw is ejected from the joint either by an SMA actuator or a regular compression spring, thus ensuring panel separation. A newly developed and now commercially available Cu-Al-Ni based SMA with a phase transition temperature above 200 °C is chosen as material for the SMA actuator, as it is compliant with ECSS regulations for space mechanisms [12]. This makes the alloy a good candidate to combine with existing D4D technologies which make use of a low melting point.

To achieve a good compromise between displacement capabilities and achievable force needed to eject the screw through the highly viscous molten PEI material, a helical spring is chosen as actuator shape.

### 3.3 T-Joint Design

The concept of the T-Joint involves passing a screw through a base insert of the clearance type, attached to one panel, and subsequently securing it to a side insert made from PEI, which is attached to the other panel using a film adhesive. The side insert design was taken from a study conducted by Kim and Lee in 2009, where they reduced the structural mass of the STSAT II satellite from 34.6% to 23.6% by eliminating a substantial number of frames used in their baseline configuration, partly by employing this novel insert [13]. The base insert houses the actuator. Figure 3 shows the cross-section of the T-Joint concept with a component description.

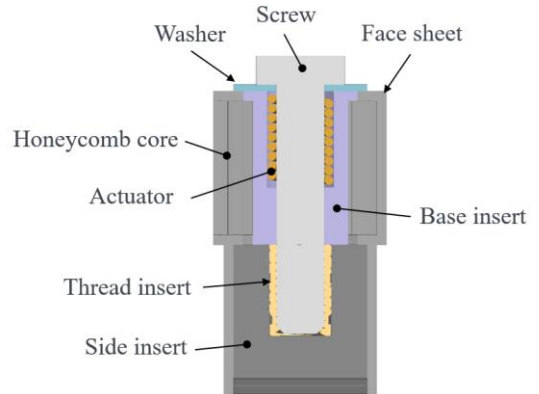


Figure 3. T-Joint Concept with component description.

Typical pre-load tensions of bolted connections in large satellite structures commonly exceed the mechanical strength of plastic threads. Consequently, the mechanical interface between the metal screw and the PEI insert has to be improved. This can be achieved by embedding an additional metal thread within the side insert. It should feature a regular metric thread on the inside, matching with screw, and a more complex geometry, achieving a form-fit connection with the PEI material on the outside. For this purpose, a COTS part of the company Ruthex™ is used. Manufactured from brass, they are exclusively made for AM applications and feature opposing spiral

knurled nuts on the outside that ensure a balanced high tightening and loosening torque, as well as high clamping force.

When utilizing an SMA actuator for the HDJ, no pretension is applied during the satellite's operational life. This reduces the overall load on the bolted connection. Expansion occurs only at elevated temperatures during re-entry, preventing unintended premature separation. A regular compression however increases reliability due to the largely reduced complexity of the actuation.

The design accounts for the satellite's tumbling motion and uneven heating, leading to non-simultaneous screw ejections. As a result, the risk of panels becoming stuck due to non-simultaneous ejections is eliminated, ensuring a reliable and predictable break-up process.

### 3.3.1 Characterisation Testing

The T-Joint design requires testing to determine the specifications for the actuator. The key goal is to find the minimum force needed to extract the screw and thread insert from the weakened PEI material. Factors affecting this include carbon fiber content of PEI, actuator and insert head diameter, screw size, retraction speed, thread insert type and specimen temperature. To ascertain the influence of the topology in the PEI – metal interface, self-tapping steel thread inserts were utilized in addition to the Ruthex inserts. A tensile test in a temperature-controlled environment is conducted to measure the maximum extraction force  $F_{max}$ .

The metallic thread inserts are embedded into the test specimen using a soldering iron. The experiment is conducted using a Zwick Retroline 1475 tensile machine with a 2 kN load cell. A threaded rod is clamped to the machine, securing the specimen on an aluminum plate with holes of different diameters. This ensures smooth extraction without extra friction. A 95 cm long threaded rod minimizes mechanical torque and heat transfer. A thermocouple is attached to the specimen to measure its temperature during testing. After setup, an oven encloses the specimen, allowing the clamps to pass through cutouts. The oven heats the specimen to the target temperature before testing. Figure 4 shows the test setup.

The exact transition temperature of the SMA material could not be determined due to material unavailability at the time of testing, so the baseline testing temperature was based on manufacturer data, with  $A_s$  around 225 °C and  $A_f$  around 245 °C (austenitic start and finish temperatures). To optimize efficiency,  $A_s$  should be close to the glass transition temperature of PEI, but since PEI's strength decreases further after  $T_g$ , a trade-off between efficiency and SMA requirements is necessary. A baseline specimen temperature of 225 °C is chosen to

account for a conservative  $F_{max}$  value.

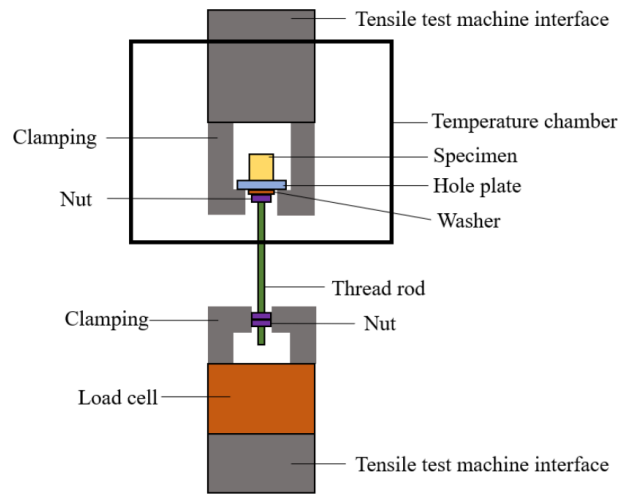


Figure 4. Tensile test setup

Table 2 lists the varying parameters identified for the test of a total of 33 specimen. The parameter values were selected to ensure broad applicability of the HDJ.

Table 2. Varied parameters for the characterization experiments.

Parameter	Variation
Screw size $d_s$	M5, M6, M8
Thread insert type	Ruthex, Self-tapping
Specimen material	PEI, CF15-PEI
Retraction velocity $v_r$	10, 30, and 60 mm/min
Specimen temperature $T_{specimen}$	180, 200, 225 °C

For the baseline configuration, a value of 10 mm/min for the retraction velocity of the lower clamping is chosen. The goal of this initial comparison is to ascertain the influence of screw size, material, and insert type. Table 3 shows the results for this baseline configuration.

The results indicate that material choice has the greatest impact on  $F_{max}$ . Post-test analysis reveals greater deformation in PEI compared to CF15-PEI due to the added rigidity of carbon fibers. PEI adheres to the thread insert during extraction, whereas CF15-PEI remains fixed, leading to a significant force increase. Figure 5 shows the evolution of the force  $F$  with respect to the displacement  $s$  for a M8 screw and a ruthex insert.

Table 3. Tensile test results for the baseline configuration,  $v_r$  is set to 10 mm/min and  $T_{specimen}$  to 225 °C

Material	Screw size	Insert type	$\overline{F_{max}}[N]$
PEI	M5	Ruthex	11.95
	M6		12.40
	M8		17.91
	M5	Self-tapping	10.62
	M6		13.89
	M8		22.50
CF15-PEI	M5	Ruthex	143.65
	M8		548.35

Individual comparisons were then carried out for the variation of specimen temperature and retraction velocity. The results indicate the second and third largest influence on  $F_{max}$ , respectively. While only a slight increase is observable for 200 °C, the force drastically increases when reducing the temperature to 180 °C, below the glass temperature of PEI.

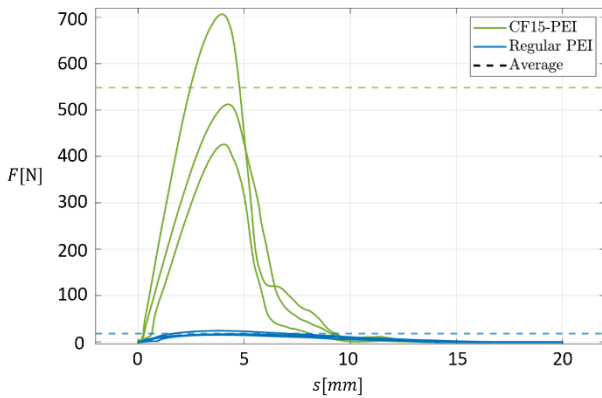


Figure 5. Force with respect to clamping displacement. Material comparison, M8, Ruthex insert, 10 mm/min, 225 °C.

### 3.4 Bracket Design

Corner connections of sandwich panels are typically realized through a bracket. Applying the presented T-Joint concept to a corner connection arises geometric difficulties resulting from the minimal edge distance of the insert. The recommended practice is to uphold a minimum distance from the edge equivalent to at least two insert head diameters [14]. Modifying the dimensions of the brackets allows for adaptation of the inserts' edge distance. Figure 6 shows the concept of the demisable joint for a bracket connection. Here, the bracket is fastened to the stationary panel with a regular threaded insert and to the separating panel with the HDJ. The functionality resembles the T-joint concept, with the key distinction being that the demisable PEI component takes the form of a washer sleeve (shown in yellow).

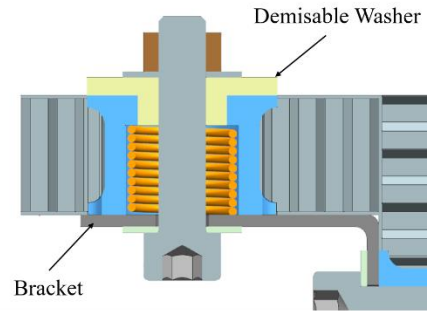


Figure 6. Concept of the demisable joint for a bracket connection.

## 3.5 Mechanical Design

### 3.5.1 Launch and Design Loads

During a rocket launch, payloads experience extreme mechanical loads, peaking in the first 20 seconds. The Falcon 9 user manual provides specific load values for quasi-static loads and eigenfrequency requirements. The HDJ's temperature-triggered mechanism remains inactive during launch, as fairing temperatures peak at 84 °C. Designed for seamless integration into S6, the HDJ does not impact global eigenfrequencies or load distribution.

For the mechanical design of S6, QSL values were increased by a 1.25 qualification factor to determine structural loads [Airbus DS]. Its bolted connection follows existing joint specifications, using M8 screws for primary sandwich panels. Table 4 shows the maximum design loads acting per screw.

Table 4. Maximum design loads acting per M8 screw for the primary structure of S6 [Airbus DS].

Force	Value [N]
$F_{ax}$	500
$F_{sh}$	4000

Due to the geometry and load distribution, the slippage margin is more relevant for the structural integrity of the connection, than the axial load on the screw. The minimum required clamping force is dependent on the number of load-transmitting screws. The total design load  $F_{tot}$  acting on the interface consist of the clamping force and the axial force and is given in Table 5 for different screw numbers  $z$ .

Table 5. Total pretension design load acting on the HDJ interface for  $z$  between 1 and 4.

$z$ [-]	$F_{tot}$ [N]
1	19,547.6
2	10,023.8
3	6,849.2
4	5,261.9

A reasonable increase in  $z$  consequently enhances the design freedom and promotes the use of high-performance thermoplastics like PEEK and PEI.

### 3.5.2 Final Designs

The designs were refined through iterative mechanical simulations in ANSYS. Material selection for each component was determined, and the interface's load-bearing capacity was evaluated. Component iterations followed system-level requirements and sandwich-panel insert design guidelines [15]. Figure 7 shows the final design of the two panel connections.

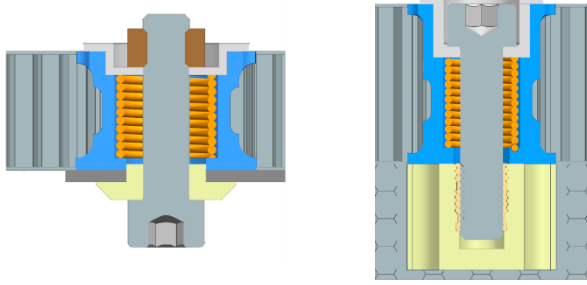


Figure 7. Final iterations of the bracket design (left) and the T-joint design (right).

### T-Design

The results show that the interface can withstand the design load without exceeding material limits only when using four screws, which corresponds to a load of 5261.9 N. The washer sleeve is made from aluminium 7075, because stresses exceed the maximum yield strength of CF30-PEEK. The maximum Von Mises stress within the base insert, made from CF30-PEEK, reaches a value of 52.87 MPa, which corresponds to a factor of safety (FoS) of 1.82.

Furthermore, the simulation results suggest using CF15-PEI as material for the side insert, as stresses exceed limitation of regular PEI when subjected to the design load. In the final iteration, a value of 70.62 MPa is reached for  $\sigma_{max}$ . The maximum stress is concentrated in a small area, likely due to numerical exaggeration near the load introduction. To verify realistic values, additional tensile tests have been conducted to measure the interface's strength at room temperature (22 °C).

The tensile test followed the setup from Sec. 3.3.1 without using an oven. Specimens were made using the same method, with material (CF15-PEI or standard PEI) as the only variable. A low retraction velocity of 2 mm/min was used to determine the maximum static force. Ten specimens (five per material) were tested with an M8 and Ruthex insert configuration. The results are shown in Table 6 and suggest, that the previous assumption regarding the numerical inflation might have been correct. The HDJ-T can theoretically withstand at least 7100.37 N for PEI and 9528.55 N for CF15-PEI.

Applying a 0.9 safety factor, the final values are 6390.33 N and 8575.70 N, respectively.

Table 6. Results of the room-temperature tensile rupture test for the thread insert interface.

Material	$F_{max}$ [kN]	$\overline{F_{max}}$ [kN]
PEI	7.41	7.34
	7.10	
	7.29	
	7.40	
	7.50	
CF15-PEI	9.92	10.00
	10.40	
	10.10	
	9.53	
	10.04	

Figure 8 shows cross-section micrographs of the tested specimens, with CF15-PEI on the left and PEI on the right. Both materials exhibit good contact with the Ruthex insert, though small air pockets are present in the insertion direction. The main difference is porosity: CF15-PEI has numerous air inclusions across the cross-section, while PEI does not. Porosity decreases about 1 mm from the thread insert, likely due to air displacement during insertion of the insert. A gray value analysis determined a 29.41% porosity level in CF15-PEI, significantly higher than the expected 2%, suggesting that reducing this value could further improve mechanical strength.

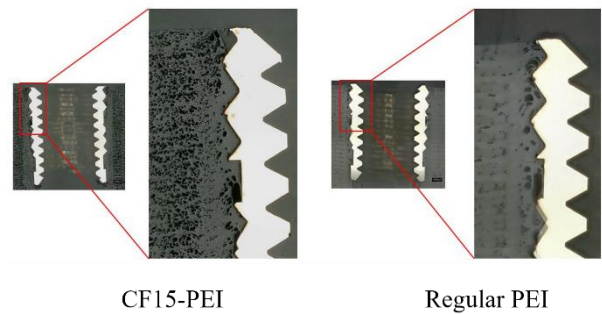


Figure 8. Micrographs of the cross section of the metal-thermoplastic interface within the side insert for CF15-PEI (left) and regular PEI (right).

### B-Design

The iterative design process of the HDJ-B was carried out in multiple steps, similar to the T-design. Initially, the design was adapted to fit the reference satellite. The first simulation showed that the structure could withstand a design load of  $F_{tot,z=3}$ , but improvements were needed to ensure simultaneous screw ejection. Adjustments were made by repositioning the demisable washer and optimizing the material selection. Further iterations

refined the fastening method, reduced unnecessary material, and improved stress distribution. The final design incorporates a washer sleeve made from stainless steel, a demisable washer (DW) made from CF15-PEI, and a base insert (BI) made from CF30-PEEK. The bracket is made from aluminium 7075, identical to the ones within S6. Table 7 shows the maximum Von Mises stresses within the components with their respective FoS.

Table 7. Static mechanical simulation results of the final iteration of the HDJ-B.

Load [N]	Component	$\sigma_{\max}$ [MPa]	FoS [-]
$F_{tot,z=3} = 6,849.2$	BI	85.30	1.13
	DW	82.26	1.13
	Bracket	140.35	2.85
	Sleeve	598.80	1.97

### 3.5.3 Shape Memory Alloy Actuator

Utilizing an SMA actuator can provide multiple advantages over a regular compression spring: it prevents additional pre-loading stress to the interface, reduces creep risk and risk for premature joint failure, and could increase break-up altitude. Unlike standard SMAs like Nitinol, the Cu-Al-Ni alloy operates at higher temperatures of  $> 200$  °C suited for space applications. The actuator dimensions were determined based on panel constraints and extraction load requirements. Due to cost constraints, extensive material testing was not conducted, but calculations confirmed that a 1.4 mm wire could generate a sufficient force of 70.79 N, significantly surpassing the required force  $F_{max} = 17.91$  N to extract the screw from the PEI side insert within the T-joint connection. After receiving detailed material data, final design adjustments were made, ensuring the SMA meets performance requirements. Table 8 lists the material properties of the copper SMA [Nimesis].

Table 8. Material properties of the utilized CuAlNi alloy.

Property	martensite	austenite
Density $\rho$ [g/cm <sup>3</sup> ]	7.1 – 7.3	
Thermal Conductivity [W/(mK)]	30	75
Young's Modulus E [GPa]	20	25
Ultimate tensile strength [MPa]	800	
Transformation range $\Delta T$ [°C]	10-30	

The spring performance is analyzed using the method of Follador et al. [16], treating the SMA actuator as a spring with two phase-dependent spring rates ( $K_m$  and  $K_a$ ). The model applies Castigliano's theorem to determine spring stiffness and maximum force, depending on wire diameter ( $d$ ), spring diameter ( $D$ ), number of coils ( $n$ ), and material properties. The Poisson ratio  $\nu$  is estimated based on alloy composition, yielding a value of 0.346. The maximum shear stress is approximated as  $R_m/2$  for assuming a simple loading tensile condition and an angle

of 45° to the direction of maximum stress, as well as a linear elastic behaviour and adopts a value of 400 MPa. The shear modulus  $G$  is calculated with Eq. 4, spring stiffness with Eq. 5, and maximum force with Eq. 6.

$$G = \frac{E}{2(1 + \nu)} \quad (4)$$

$$K = \frac{Gd^4}{8nD^3} \quad (5)$$

$$F = \frac{\tau_{max}\pi d^3}{8D} \quad (6)$$

The model shows that increasing wire diameter raises the maximum force, while increasing spring diameter reduces it. The total wire length is 477 mm for the T-spring and 490 mm for the B-spring. The axial lengths in retracted ( $L_m$ ) and expanded ( $L_a$ ) states are set to ensure proper separation of panels. The final coil is ground to improve contact with the sleeve and align perpendicularly to the screw axis. Table 9 list the values of the above parameters.

Table 9. Geometric parameters and resulting spring properties.

Parameter	HDJ-T	HDJ-B
$d$ [mm]	1.4	
$D$ [mm]	12.5	15.6
$n$ [-]	11.72	9.65
$K_m$ [N/mm]	0.623	0.390
$K_a$ [N/mm]	0.701	0.438
$F$ [N]	34.48	27.63
$L_m$ [mm]	17	14
$L_a$ [mm]	32	27

The results confirm that the spring force is sufficient for screw ejection. Since no other established methods exist for SMA spring assessment, an experimental approach will be conducted once the material is available (detailed in Sec. 5.1). Differential scanning calorimetry (DSC) results of the acquired material confirm the phase transition temperatures, with  $A_s = 199.06$  °C and  $A_f = 220$  °C, aligning well with the design assumptions.

## 4 SIMULATIONS

### 4.1 Re-entry Analysis and Fragmentation Strategy

This section presents system-level re-entry simulations using the S6 reference model to evaluate the impact of the newly designed HDJ on satellite break-up and DCA. The goal is to determine the most effective HDJ implementation to increase break-up altitude and DCA.

The DCA values in this study are independently calculated and do not reflect actual S6 mission data.

The passive HDJ promotes early disintegration, allowing airflow to accelerate demise. Not all conventional joints need replacement; selected panels are detached when a temperature threshold is reached. To analyze this, different model variations are created, each using HDJs on specific panels.

Re-entry simulations are conducted using SCARAB, which models satellite structures and analyzes flight dynamics, aerodynamics, heating, thermal and structural behaviour, and fragmentation. The tool calculates satellite break-up based on thermal fragmentation, with mechanical failure considered in specific cases [17]. After a simulation, SCARAB generates reports summarizing input data, re-entry history, event summaries, and impact analysis, providing insights into satellite break-up behaviour and casualty risk.

### Model Setup and Parameter Identification

Due to the complexity of modeling detailed geometries in SCARAB, HTG provided a simplified S6 satellite model for the re-entry analysis in this study, with Airbus DS supplying the necessary data. The model includes all major structural components and material data. The re-entry analysis begins by defining initial simulation parameters and selecting appropriate boundary conditions, which significantly influence the results.

The DCA is calculated based on the projected surface area of surviving fragments using Eq. 7. Fragments with impact energy below 15 J, computed via Eq. 8, are excluded from the DCA calculation.

$$DCA = \sum_{i=1}^N (0.6 + \sqrt{A_i})^2 \quad (7)$$

$$E_{imp} = \frac{1}{2} \cdot m_{frag} \cdot v_{impact}^2 \quad (8)$$

The initial state of the satellite is defined by its orientation, position, velocity, and re-entry time. Since orientation is not varied in this analysis, rotational motion is set to zero. The orbit is specified using Keplerian elements, with an eccentricity of 0.001 and an inclination of 66.0341°. Other orbital parameters are set to zero, ensuring the simulation always starts over the equator. The semi-major axis  $a$  must be carefully chosen, as the breakup phase above 100 km altitude is crucial for the study.

A larger  $a$  value extends exposure to atmospheric forces, promoting satellite demise. The standard value is 6510 km (125 km altitude), where atmospheric effects become noticeable. However, an initial simulation with this value

took about five days to compute. To save resources, a second simulation used  $a = 6495$  km (110 km altitude), reducing computation time to two days. presents the simulation results for the baseline model. The definition of the break-up altitude refers to the first fragmentation event of the main object.

Table 10. Re-entry analysis results for the baseline configuration with varying semi-major axis.

Case	$a$ [km]	Break-up alt. [km]	DCA [ $m^2$ ]
FM-001	6510	97.5	9.996
FM-002	6495	101.9	10.746

To reduce the overall computation time, a value for the semi-major axis of 6495 km is chosen as fixed for the variant comparison. The trajectory depicted is computed until the end of the melting phase for  $Ma > 6$ . It is important to mention, that the error of the computed DCA is around 13%.

The simulation accounted for third-body gravitational effects from the sun and moon, as well as solar radiation pressure, using the MSISE-90 atmospheric model. A mass correction factor of 1.01 was applied to match the panelized model's mass with the reference satellite's dry mass. The total mass was set at 990.5 kg and kept constant across all model variations for result comparability.

A minimum fragment mass (MFM) of 0.3 kg was chosen to prevent numerical errors. It had to be at least three times the maximum mean panel mass of any model component to avoid the "ballooning effect," where fragments lose mass without shrinking, causing them to unrealistically remain airborne instead of reaching the ground.

### Separation Scenarios Modeling

Since the HDJ cannot be modeled in detail, it is substituted using a dummy element. The dimensions of this dummy are chosen according to the height and thickness of the classic bracket joint and adopt values of 50 mm and 2 mm respectively. The separation event is simulated by defining a primitive whose temperature is monitored during re-entry. When a predefined temperature threshold of a conservative value of 250 °C is reached, the separation of arbitrary primitives is triggered.

In order to assess the effect of the separation of different panels of the primary structure on the demise behaviour, six modified variants were identified. Figure 9 shows an over-simplified model of S6 with specifications of the individual panels comprising the outer primary structure.

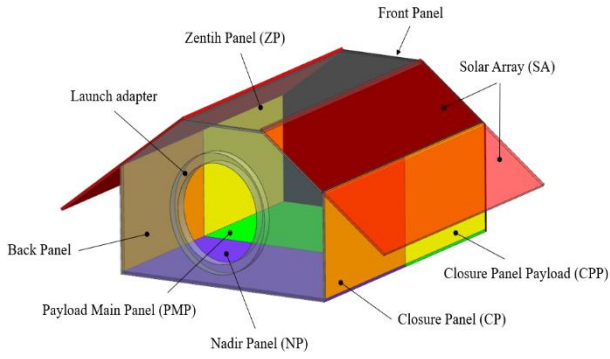


Figure 9. Over-simplified model of the outer structure of S6 (not to scale).

Table 11 lists six variants selected for comparison to the baseline model. They were chosen based on feasibility, determined by the number of attached elements per panel. Due to limited data, a detailed feasibility analysis was not conducted. However, variants A, B, C, and D are considered more feasible than E and F, particularly regarding the harness, which is excluded for simplicity.

Table 11. Definition of the modifications to the baseline model.

Variant	Separating panels	N° of panels
A	CP	2
B	CP, CPP	4
C	SA	4
D	CP, CPP, SA	8
E	NP, PMP	2
F	CP, CPP, SA, NP, PMP	10

## Results

Variants F, C, and D experience separation much earlier than the others, occurring at 365, 394, and 601 seconds, respectively. Variants B, A, and E follow at 1316, 1348, and 1411 seconds. In the reference case, the first panels melt at 1324 seconds. Differences in trajectory result from varying aerodynamic effects caused by panel separation. Figure 10 shows the trajectories of variants A-F in comparison with the baseline case FM-002 together with the initial separation event and the first thermal fragmentation for the baseline model.

A slower descent rate extends the melting phase since less energy dissipates in the thinner upper atmosphere, delaying deceleration. This causes melting to occur at lower altitudes. The satellite's tumbling motion, influenced by aerodynamic forces, affects surface heating. S6 tends to align slightly with its motion direction due to its roof-shaped solar panels, leading to uneven heat distribution. For example, in variant C, at 385 seconds, the solar panels are still attached, with a 200°C temperature difference between the nadir and

zenith faces. By 397 seconds, one solar panel detaches as its bracket reaches 250°C, and the second separates at 544 seconds.

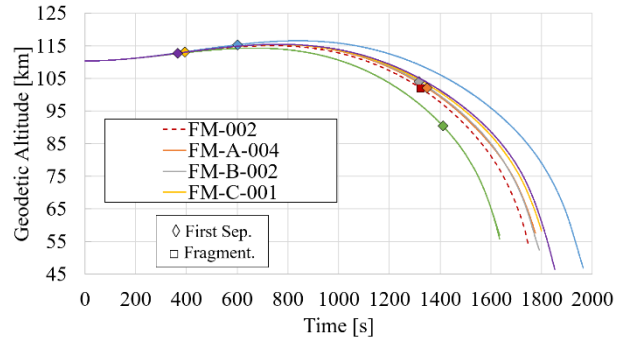


Figure 10. Trajectories of variants A-F with baseline case FM-002.

Table 12 presents the casualty areas and separations altitudes for all variants. As expected, variants C, D, and F show the most improvement over the baseline, with values of 7.239, 8.003, and 7.819 m<sup>2</sup>, respectively. Variant C features the greatest reduction at a value of around 32%.

Table 12. Results of the comparative study. Separation threshold temperature of 250°C, semi-major axis of 6495 km.

Variant	Trigger dur. [s]	Sep. alt. [km]	DCA[m <sup>2</sup> ]
0	-	-	10.746
A	1348	102.14	10.001
B	1316	104.00	10.272
C	394	113.04	7.239
D	601	115.33	8.003
E	1411	90.42	10.491
F	365	112.75	7.819

Separating only the large nadir-side panels does not significantly reduce the overall DCA due to their late detachment caused by slower heating. Although variant F combines all other modifications and has the earliest panel separation, it does not achieve the lowest DCA. The difference between variants A and B in both DCA and break-up altitude is minimal. Since the DCA includes all surviving fragments that reach the ground, it is important to analyze their origin and how each variant affects component demise. Some satellite components are harder to destroy due to their material properties and shape, making them more likely to survive re-entry.

Figure 11 compares the casualty areas of key components, including the AMR-C instrument, magnetorquers (MTQ), reaction wheels (RWL), the mono-propellant propulsion system (MPPS), the tank, and batteries, across all variants. The baseline model had an additional primary structure fragment with a DCA of

0.435 m<sup>2</sup>, which is excluded from the figure.

The results show that not all components are affected equally. The titanium tank remains unchanged, while the battery sees little change in cases A through D but higher DCA in variants E and F, indicating reduced demise. The RWL contributes most to the overall DCA, with improved demise in cases B, C, D, and especially F. The MTQ is completely destroyed in variants C and D but performs worse in case B. The AMR-C shows improvement across all variants, with the biggest reduction in variants E and F.

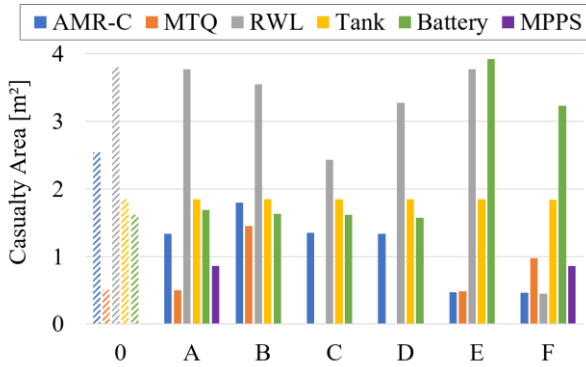


Figure 11. DCA of the most relevant surviving components.

Additional re-entry simulations were conducted for selected variants to assess the influence of certain parameters on the DCA. These tests lowered the detachment threshold temperature to 225 °C and used a semi-major axis of 6510 km.

The results showed that lowering the trigger temperature and increasing simulation altitude caused separation at slightly higher altitudes in all cases, as expected. For variants A, C, and D, simulations at a starting altitude of 125 km were performed. In variant D, solar panels detached earlier than in variant C, leading to increased heating of connected joints and earlier detachment of additional components.

Due to time constraints, only selected cases were compared. The results aligned with the previous study, with variant D now showing the greatest improvement. The DCA for variant D was significantly lower at 3.966 m<sup>2</sup>, which corresponds to a reduction of around 60% compared to the reference case at a starting altitude of 125 km. However, variant A unexpectedly showed an increased DCA, possibly due to simulation uncertainties.

Overall, the study confirms that replacing traditional joints with targeted alternatives can significantly improve satellite demise.

## 4.2 Thermal Transient Simulations

Thermal simulations using Ansys evaluated heat distribution in the HDJ during re-entry, focusing on the

SMA actuator and PEI part. SCARAB provided atmospheric temperature and heat flux data along the trajectory. The provided heat flux is occurring at the stagnation point. Due to the satellite's irregular tumbling motion, the heat flux varies over its surface, introducing some uncertainties. The heat transfer rate depends on the angle  $\theta$  between the surface and airflow. Using this, the total heat flux over a sphere's surface can be integrated. The surface heat flux is then determined using the average projected area theorem, which states that for a convex 3D body, the average projected area is one-fourth of the total surface area. For a sphere, this is evident since its total surface area is  $4\pi R^2$  and its projected area is  $\pi R^2$ .

To compare the thermal simulation with the re-entry analysis, the relevant data was used for each case. Baseline cases FM-001 and FM-002 were analyzed to assess how the starting altitude affects heating. To save computing resources, only the early re-entry phase was simulated. For FM-001, the simulation ran down to 95 km (time step 3977 s), while for FM-002, it covered the first 1508 s, reaching 90 km altitude.

Thermal transient simulations were conducted using two finite element models, one for the T-design and one for the B-design. To simplify the model, the surrounding sandwich panel was omitted, as its minimal mass is considered to have little effect on heat distribution.

Table 13 lists the emissivity, thermal conductivity, and specific heat capacity of the materials used, based on the final mechanical design. Temperature-dependent data was only available for CF30-PEEK, while other materials used values at 20°C.

Table 13. Thermal properties of materials utilized in the thermal transient simulations.

Material	$\epsilon$ [-]	$\lambda$ [W/mK]	$c_p$ [J/kgK]
Aluminium 7075	0.1	145	862
Titanium Grade 5	0.2	7.1	560
CF30-PEEK	0.9	-	-
PEI	0.9	0.24	1534
CuAlNi	0.06	30	473
Brass	-	121	377
Steel	0.1	60.5	434

The SMA spring actuator's complex helical shape caused meshing issues, so a simplified model with adjusted density and thermal conductivity (50% lower) was used for the HDJ-B model. A similar approach was taken for the HDJ-T model after accuracy concerns. A refined mesh test for case showed a variation of only 0.98%, confirming the chosen mesh size's validity.

## Results

The thermal transient simulations focused on evaluating

the heating characteristics of the HDJ designs by monitoring key threshold temperatures. Specifically, the analysis examined the time required for the PEI component to reach its glass transition temperature of 186 °C, as well as the SMA actuator to reach the austenitic finish temperature, both at its maximum and minimum temperature points. A value of 225 °C was chosen according to the DSC results of the CuAlNi-alloy and to enable better comparability with performed re-entry analyses. By comparing these heating durations with the observed separation behaviour in the re-entry analysis, the realism and accuracy of the results were assessed.

The characterisation tests demonstrated that the required extraction force for separation decreases significantly once the PEI reaches 186 °C. The SMA actuator, however, must reach 225°C at its coldest point for complete separation to occur. A key observation from the simulations was that the PEI component, positioned farther from the direct heat flux, exhibited longer heating durations than the SMA actuator despite having a lower activation temperature. This difference led to variations in the predicted break-up altitudes. For HDJ-T design, cases where the PEI was the determining factor, the separation altitude was approximately 92 km, whereas an altitude of 103 km was obtained when considering the SMA actuator. These findings indicate that optimizing heat conduction within the structure could lead to a more uniform heating process, thereby affecting the break-up altitude.

Comparing the two HDJ designs, the HDJ-B model exhibited slightly reduced heating durations compared to HDJ-T, resulting in a higher separation altitude of approximately 98 km. When using input data from case FM-001 (125 km altitude), the separation altitude for HDJ-B increased further to 108.5 km. The computed average break-up altitude across all cases was 99.5 km. This closely aligns with results from re-entry simulations, which included variants A, C, and E (variants with distinct separating panels), which result in a mean break-up altitude of 103.4 km for a trigger temperature of 225°C. The minor discrepancy of 3.9 km between the thermal transient simulations and the re-entry simulations provides a broad validation of the findings from the re-entry simulations.

## 5 DEMONSTRATOR

### 5.1 Manufacturing

To ensure reliable testing results, the demonstrators were designed to closely match the sandwich structure of the reference mission using comparable materials. However, the specified aluminum honeycomb core was unavailable in small quantities and too costly. As an alternative, an additively manufactured CF30-PEEK core was used, chosen for its ability to withstand high temperatures

while being cost-effective and easy to produce. The core was fabricated with a 15% honeycomb infill, and cavities were left for potting material to bond the inserts.

Key components were 3D-printed from CF30-PEEK and PEI. Since the test focused on thermal behaviour rather than mechanical loads, the regular threaded insert within the static panel in the HDJ-B design was replaced with a 3D-printed insert reinforced with a Ruthex thread.

### SMA Spring Fabrication

The manual fabrication of SMA springs plays a crucial role in the design process, allowing for cost-effective prototyping. The actuator manufacturing method follows the approach proposed by Follador et al. (2012) and ensures repeatability among different actuators [16]. To program the desired shape in the austenitic phase, the springs are mechanically constrained and heat-treated at 450 °C for 30 minutes, followed by water quenching. The springs are initially formed in an expanded shape and later plastically deformed into the contracted assembly state.

The fabrication setup consists of aluminum blocks, a central rod, and a clamping mechanism to secure the wire. It is wound around the rod with controlled coil spacing before being heat-treated. Two setups were used to accommodate the T- and B-spring designs. However, inconsistencies in the provided wire, reduced total usable length, brittleness and surface defects which led to breakage, limited the successful spring production. Figure 12 shows the fabrication setup in an oven and the post-heated springs.



Figure 12. Spring fabrication setup inside the oven before heating (left). SMA springs post-heating (right).

Following heat treatment, the springs exhibited unexpected stiffness and lacked plastic deformability in the contracting direction. When compressed, they returned to an elongated shape instead of maintaining deformation, resembling the behaviour of a regular compression spring. Attempts to plastically deform them by applying tension resulted in material fracture. After mechanical constraint over several days, slight creeping was observed, with the SMA-T and SMA-B springs contracting from 35 to 27 mm and from 28 to 22 mm, respectively. A total of 4 specimen could be successfully manufactured.

The deviations in expected behaviour suggest suboptimal production quality or heat treatment inconsistencies.

Future work requires closer collaboration with material manufacturers to improve quality. Due to delivery delays and material shortages, further characterization was not feasible, leading to the integration of both regular compression springs and SMA actuators into the prototypes. The compression springs feature pretensions in the assembly state of 26.45 N and 50 N for the T- and D-design, respectively.

### Assembly

The prototype assembly begins with bonding the facesheets to the honeycomb cores using Loctite™ EA 9695 Aero epoxy film adhesive. The adhesive is cut to shape, placed between the facesheet and core, and aligned with the edges and holes. The assembly is then loaded with an adjustable wrench for uniform bonding and cured in an oven at 120 °C for one hour. After cooling, the BI's and threaded inserts are positioned, and the epoxy potting compound GP 49 is injected into the cavities using a pressurized glue gun at 6 bars. Once the sandwich structure is complete, the panels are assembled by inserting the actuators and washer sleeves into the BI, securing them with screws and nuts. Figure 13 shows the assembly process.

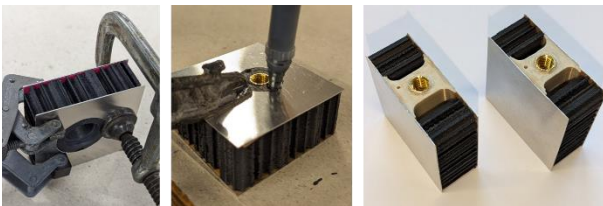


Figure 13. Assembly process of the sandwich panels.

### 5.2 Prototype Testing

The experiment aims to verify the functionality of the passive screw ejection mechanism and determine the temperature at which separation occurs. Since the exact heat flux during re-entry cannot be replicated, the aim is not to validate thermal transient simulations, but to measure the mechanisms activation temperature. Four samples are tested: both the T- and B-design, each with

one variant using an SMA actuator and one using a compression spring.

Type K thermocouples are attached to the assembly, ensuring proper insulation to avoid measurement errors. The temperatures of the PEI components and the SMA springs are recorded. For prototypes with an SMA actuator, a thermocouple is attached to the lower end of the spring using polyimide tape, while a slot in the BI allows the thermocouple wire to pass through. For the T-design, the SI temperature is measured via a drilled hole, while the DW temperature is measured on the surface to avoid structural weakening. Since the test does not involve mechanical loads, screws are hand-tightened rather than pre-tensioned.

After assembly, the oven is heated to 300 °C, and the prototypes are placed inside. A Graphtec GL840 records temperature data, while a video camera captures the mechanism's response. The video is later synchronized with the temperature data to analyze the timing of the screw ejection. Figure 14 shows the four specimens before testing.

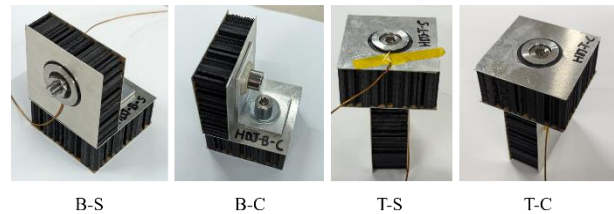


Figure 14. Prototype assemblies with integrated thermocouples before oven testing.

### Results

#### HDJ-B:

Figure 15 presents the temperature measurements of the bracket prototypes: the SMA actuator is shown on the left, and the compression spring on the right. The start and end times of the dynamic screw ejection are marked with blue and orange dashed vertical lines, respectively.

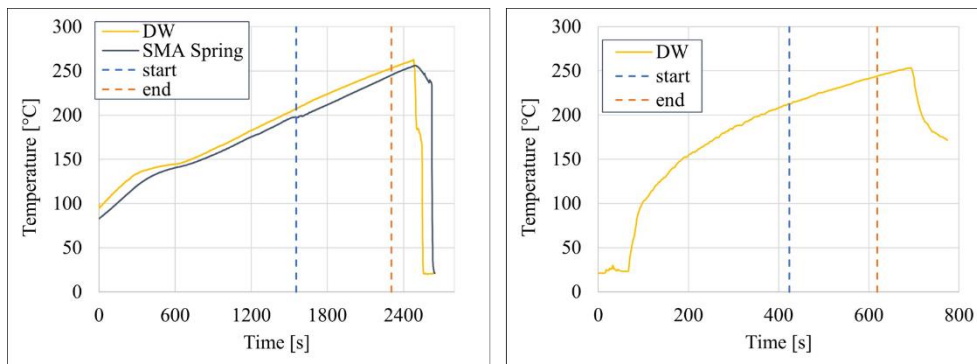


Figure 15. Temperature curves over time for the B-S prototype (left) and B-C (right) with start and end of the screw ejection mechanism marked with dashed lines

A slight difference between the SMA spring and DW temperatures can be observed in the HDJ-B-S case due to delayed heat conduction within the joint assembly. For the HDJ-B-S model, the mechanism is triggered at  $t_s = 1554$  s with  $T_{DW} = 207.3$  °C and  $T_{SMA,s} = 197.7$  °C, taking 751 s to complete, reaching a maximum stroke of the SMA spring at  $T_{SMA,e} = 245.4$  °C. In contrast, for the B-C model, the activation occurs at  $t_s = 424$  s and  $T_{DW} = 212.6$  °C, with a duration of only 195 s. This difference is partly due to a lower oven temperature during the B-S test, as the oven was not fully pre-heated to 300 °C. A key comparison is the activation temperature. Given that the spring force in the SMA spring assembly (3.12 N) is much lower than that of the compression spring (50 N), one would expect the compression spring to activate at a lower temperature based solely on spring force. However, with the DSC peak at 199.1 °C for  $A_s$  and the phase transition starting slightly before this point show, that the SMA actuator generates enough force to trigger the ejection process earlier than the compression spring. The compression spring finishes the movement after a temperature change of 31.2 °C, while the SMA spring takes 45.9 °C, but with a larger stroke. Figure 16 shows the B-S (left) and B-C (right) models after testing.

In both cases, the screw head was successfully ejected through the bracket hole, separating the panels. The compression spring extended enough to remove the screw, but due to its cutback, it became jammed with the sleeve, preventing the screw from entirely falling off. After testing, the B-design SMA spring was measured at 25.1 mm, indicating that the shape memory effect (SME)

occurred, providing an elongation of 3.1 mm from its original 22 mm. Combining the SME and spring elongation, the B-SMA actuator provided a total elongation of 11.1 mm.



Figure 16. Ejected screw and separated panels of the B-C sample after testing.

### HDJ-T:

Figure 17 presents the results of the HDJ-T prototypes, with the T-S sample on the left and the T-C sample on the right. The start and end times of the screw ejection are marked similarly to the bracket design. For the T-S model, ejection starts at 718 s with  $T_{SI} = 205.9$  °C and  $T_{SMA,s} = 191.8$  °C, completing in 728 s when  $T_{SMA,e}$  reaches 273.3 °C. In contrast, the T-C model starts at 798 s with  $T_{SI} = 233.5$  °C and completes in 196 s. The extraction duration is similar across both designs, but heating gradients differ, even though the oven was held at 300 °C in both cases. Activation temperatures show trends similar to the B-design, confirming previous assumptions. The SMA actuator applies significantly less force than the compression spring (6.23 N vs 26.45 N) – solely from spring pretension – yet initiates extraction earlier due to phase transformation.

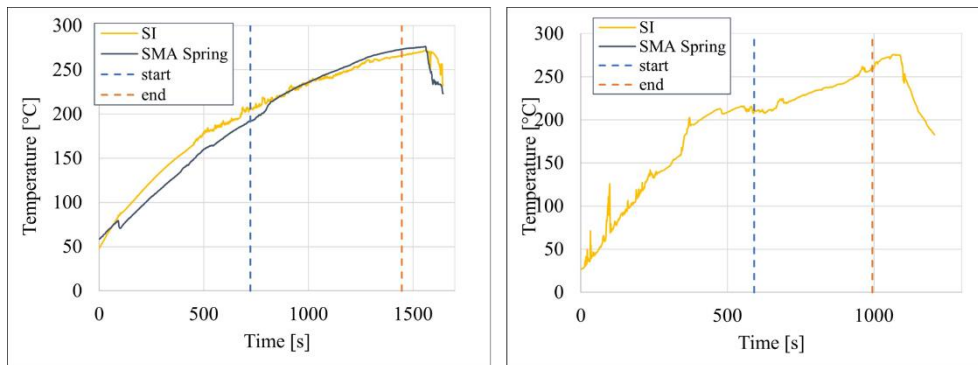


Figure 17. Temperature curves over time for the HDJ-T-S prototype (left) and HDJ-T-C prototype (right) with start and end of the screw ejection mechanism marked with dashed lines

The compression spring completes movement after a  $\Delta T$  of 25 °C, while the SMA spring takes 60.6 °C, despite having a larger stroke.

Figure 18 shows the post-test assemblies. In both cases, the screw and thread insert were successfully ejected, allowing panel separation. However, the T-S spring fractured at the top coil, likely due to screw tightening during assembly. After testing, the T-SMA spring

measured 34.8 mm, indicating 7.8 mm of shape memory elongation from its original 27 mm. This exceeds the B-SMA's 3.1 mm extension. In total, the T-SMA actuator achieved a 17.8 mm elongation. As seen in Figure 18 (right), the screw, thread insert, and washer sleeve were fully ejected due to spring tension.



Figure 18. Ejected screw and separated panels of the HDJ-T-S sample (left) and HDJ-T-C (right) sample after testing.

### Summary:

Overall, the mechanism starts within a PEI temperature range from 205.85 °C (T-S) to 233.5 °C (T-C). The ejection completes between 243.8 °C and 266.4 °C, with an average panel separation temperature of 255.5 °C. This outcome strongly suggests the accuracy of the re-entry analysis, considering that the separation trigger was configured at 250 °C for the baseline comparative study.

The PEI component is the limiting factor in the process. During re-entry, it remains the coolest part of the joint due to its distance from the heat source, as shown in thermal simulations. Improving the SMA spring's mechanical performance and optimizing heat conduction to the demising PEI component could lower the threshold temperature, potentially making panel separation possible at temperatures below 225 °C.

## 6 DISCUSSION AND CONCLUSION

This study developed two structural joint designs, HDJ-T and HDJ-B, to enable passive temperature-induced separation of satellite panels during re-entry. Inspired by the S6 mission's structural configuration, these joints integrate high-performance thermoplastics (PEI and CF15-PEI) and SMA or compression spring actuators to enhance spacecraft demisability.

Key findings highlight the significant impact of material selection and joint design on the required ejection force. Carbon fiber reinforcement increased force requirements drastically, while factors like temperature and retraction velocity also played a role. Mechanical analyses confirmed that both HDJ-T and HDJ-B withstand launch loads, with additional tensile tests surpassing simulation predictions. The SMA spring actuators, designed with a 200°C phase transition temperature, demonstrated effective screw ejection capability, with the B-SMA achieving an 11.1 mm stroke and the T-SMA 17.8 mm.

A system-level re-entry analysis validated the effectiveness of the mechanism in reducing the demise casualty area (DCA). Simulations using the SCARAB tool indicated that timely panel separation improves spacecraft break-up behaviour, with peak results yielding a DCA of 3.966 m<sup>2</sup> and break-up altitudes up to 115.53 km. Thermal simulations supported these findings,

aligning closely with re-entry predictions.

Prototypes were manufactured and tested, successfully ejecting screws at temperatures around 207–233°C. The SMA actuator's ability to initiate separation at lower temperatures than the compression spring suggests additional force contribution from shape memory expansion. Future work should focus on optimizing SMA spring performance and conduct thorough characterisation through thermal cycling tests and parameter refinements. The goal is to lower separation temperatures and increase break-up altitude. Additionally, incorporating higher-fidelity joint models into re-entry simulations and conducting plasma wind tunnel tests could further validate performance under realistic conditions. To enhance the mechanical strength of the joints, the metal-thermoplastic interface could be reiterated, thus increasing the load-bearing capabilities. Geometric optimizations and system-level considerations could improve the reliability of the mechanism.

In conclusion, the proposed joint designs show strong potential for improving satellite demisability while being compatible with standard sandwich structures. The combination of thermoplastic manufacturing and SMA-based actuation offers a promising approach to enhancing spacecraft re-entry safety and reducing ground casualty risk.

## 7 REFERENCES

1. ESA ESOC. *ESA's Annual Space Environment Report (2023)*.
2. ESA (2025). Space Environment Statistics. Online at <https://sdup.esoc.esa.int/discosweb/statistics/> (as of 3. March 2025)
3. Kessler D.J. & Cour-Palais B.G. (1978). *Collision frequency of artificial satellites: The creation of a debris belt*. Journal of Geophysical Research. Volume 83, Issue A6. pp2637-2646.
4. Kelley R.L. (2012). Using the Design for Demise Philosophy to Reduce Casualty Risk Due to Reentering Spacecraft. In *63rd International Astronautical Congress (IAC2012)*
5. Heinrich, S., Martin, J. & Pouzin, J. (2019). Satellite design for demise thermal characterisation in early re-entry for dismantlement mechanisms. *Acta Astronautica* **158**, pp. 161– 171.
6. Donlon, C.J., Cullen, R. & Giulucchi L. (2021). The Copernicus Sentinel-6 mission: Enhanced continuity of satellite sea level measurements from space. *Remote Sensing of Environment* **258**.
7. Patzwald, J. (2021). Design for Demise Concepts with additively manufactured satellite parts. *Master Thesis, RWTH Aachen*.

8. Brodbeck, M. (2022). Design of Demisable Joints with a passive ejection mechanism. *Bachelor Thesis, University of Stuttgart*.
9. Grassi, L., Bianchi, S., Schleutker, T., Gülhan, A. & Esser, B. (2021). Demisable Joint. *2021 Clean Space Industrial Days*.
10. Sauerbrey, M., Beck, J. & Caiazzo, A. (2021). New Demise Technology Concepts of Spacecraft Structural Joints. *ECSSMET 2021*.
11. Ring, A. (2023). Hybrid Demisable Joint Concept for High-Altitude Break-Up of Primary Satellite Structures. *Master Thesis, University of Stuttgart*.
12. Fouché, F., Hautcoeur, A. & Chassoulier, D. (2017). Development and Testing of a High-Temperature Shape Memory Actuator Using Cn-250x For Hold Down and Release Mechanisms (HRM). *ESMATS 2017, Univ. of Hertfordshire, Hatfield, U.K., 20–22 September 2017*.
13. Kim, B.J., Lee, D.G. (2010). Development of a satellite structure with the sandwich T-joint. *Composite Structures* **92**(2), pp. 460-468.
14. Shur-Lok Corporation (1996). Design Manual - Fasteners for Sandwich Structures. Online at <https://www.shur-lok.com/documents/catalogs/sandwich-structure-design-manual.pdf> (as of 20. March 2025)
15. ECSS (2011). Space Engineering Insert Design Handbook. *ECSS-E-HB-32-22A*.
16. Follador, M. et al. (2012). A general method for the design and fabrication of shape memory alloy active spring actuators. *Smart Materials and Structures* **21.11**, p. 115029.
17. Koppenwallner, G., Fritsche, B. & Lips, T. (2004). SCARAB - A Multi-Disciplinary Code for Destruction Analysis of Space-Craft during Re-Entry. *Fifth European Symposium on Aerothermodynamics for Space Vehicles (ESA SP-563). 8-11 November 2004, Cologne, Germany*

